Advanced Materials

ADVANCED MATERIALS
www.advmat.de

RESEARCH ARTICLE

Mechanical-Thermal Decoupling Engineering Unlocks Ultra-Stable Dry Thick Iodine Cathodes for Ah-Level Zinc-Based Pouch Batteries

Hengrui Guo[1,2] | Hao Luo[1,2,3] | Fulong Zhu[3] | Shunyao Li[1] | Xueying Su[1,2] | Zhenxin Chen[1] | Ao Liu[1] | Jinchi Li[3] | Wanhai Zhou[3] | Mi Lu[1] | Tiefeng Liu[4] | Yang Yang[5] | Dongliang Chao[3]

[1]School of Materials Science and Engineering, Xiamen University of Technology, Xiamen, Fujian, China | [2]School of Materials Science and Engineering, Zhengzhou University, Zhengzhou, China | [3]Laboratory of Advanced Materials, Aqueous Battery Center, College of Smart Materials and Future Energy, Fudan University, Shanghai, P. R. China | [4]Quzhou Institute of Power Battery and Grid Energy Storage, Quzhou, China | [5]State Key Laboratory of Physical Chemistry of Solid Surfaces, State-Province Joint Engineering Laboratory of Power Source Technology for New Energy Vehicle, College of Chemistry and Chemical Engineering, Xiamen University, Xiamen, P. R. China

Correspondence: Hao Luo (luohao@xmut.edu.cn) | Mi Lu (lumihit@sina.com) | Yang Yang (yangyang419@xmu.edu.cn) | Dongliang Chao (chaod@fudan.edu.cn)

Received: 28 January 2026 | **Revised:** 28 January 2026 | **Accepted:** 31 March 2026

Keywords: abnormal iodine migration | Ah-level pouch cells | aqueous zinc–iodine batteries | dry thick electrodes | mechanical-thermal decoupling

ABSTRACT

Solvent-free dry processing is ideal for fabricating thick iodine electrodes, but limited by slow kinetics and poor cycling stability. Herein, we reveal that, under continuous high-shear processing, the coupled effects of uncontrolled mechanical stress and frictional heating destroy mass-transport channels and induce silent iodine loss. Inspired by low-frequency mild mechanical actuation in respiratory systems, a targeted energy intermittent release strategy based on water-cooled pulse shearing is proposed to achieve precise decoupling and regulation of mechanical force and frictional heat accumulation. It is revealed that maintaining energy input below the thresholds of carbon host structure damage and iodine desorption, avoids micro-scale "pore-like" structure exposed to the cracking of low-crystallinity carbon, thereby preserving strong van der Waals confinement between carbon and iodine, fundamentally preventing abnormal iodine migration. Concurrently, regulating the energy within the window between PTFE fiber formation and fracture, contrasts a uniform and stable thick iodine electrode at the micro-macro scale, which enables over 50000 stable cycles at 100 C and an ultra-high area capacity of 16.27 mAh cm^{-2} based on 82.84 mg_{iodine} cm^{-2} iodine loading. Importantly, a ≈1.2 Ah pouch cell even retains 98.5% capacity after 300 cycles at 2 C, demonstrating the scalability and practical viability of the strategy.

1 | Introduction

Aqueous zinc–iodine batteries (AZIBs) have demonstrated ultra-long lifespans of up to one hundred thousand cycles in recent research, but their practical energy density remains limited (<40 Wh kg^{-1}) owing to the relatively low I_2 loading (<3 mg cm^{-2}) [1–3, 4]. Consequently, the development of AZIBs with high areal capacity while retaining prolonged cycling stability is essential for long-duration energy storage applications [5–9]. Among the available routes, constructing thick electrodes is considered one of the most direct and effective strategies [10–14]. Nevertheless, elemental iodine, which exhibits non-negligible solubility and strong thermal sensitivity, makes thick electrodes fabricated through wet-processing (WP) inevitably involve solvent exposure

and high-temperature drying steps, causing the collapse or blockage of the electrode channel and disrupting the initially microscopically uniform and stable carbon-iodine confinement state [15–20]. This not only impedes radial ion transport across the thick electrode but also aggravates polyiodide shuttle risk, ultimately resulting in both reduced iodine utilization rate and deteriorated cycling stability.

Dry electrode preparation technology eliminates the use of solvent, thereby preventing solvent-induced binder migration and reducing the energy demand associated with high-temperature drying, making it an appealing pathway for high-loading electrodes [10–12]. For cathodes that do not rely on host confinement and are thermally robust (eg. ZnI_2 [7], $LiNi_{0.8}Co_{0.1}Mn_{0.1}O_2$ [21], $LiMn_2O_4$ [22], LMO||Si/C [10]), dry processing (DP) primarily requires sufficient shear energy to induce Polytetrafluoroethylene (PTFE) fibrillation and construct a continuous 3D network. Yet applying similar high shear conditions to carbon-iodine composites can be detrimental because iodine confinement depends on intact micro/mesoporous hosts, and iodine itself is thermally unstable [15–17, 23]. Sustained high shear force continuously acts on the porous carbon host, inducing C═C/C─C bonds rupture within the low-crystallinity carbon skeleton, followed by atomic rearrangement [24–26]. This process leads to particle fragmentation and the collapse/opening of micro- and meso-scale closed pores, thereby weakening the physical confinement of the original high Van der Waals force and exposing previously encapsulated iodine [27, 28]. Meanwhile, continuous friction and extrusion among particles cause heat accumulation and transient local temperature hotspots, which further accelerate the risk of iodine desorption and loss [29]. Such processing-induced silent iodine loss is difficult to detect during electrode fabrication but is progressively amplified during subsequent cycling, ultimately resulting in capacity decay in the thick iodine electrode. Fundamentally, the transient coupling of shear-induced mechanical forces and frictional heating is a concrete manifestation of processing energy injection into the electrode in multiple forms [30, 31]. Once the rate or intensity of energy input exceeds the structural tolerance threshold of the constituent materials, degradation of the host framework and the PTFE fibrillar network, as well as the thermal destabilization of iodine species, will inevitably occur (Scheme 1a). Therefore, controlling energy input is critical for enabling thick iodine electrodes with high areal capacity and long-term stability [32].

Inspired by the physiological mechanism by which the respiratory frequency in the lungs regulates drug transport and retention, we proposed a low-temperature, intermittent energy-regulation strategy based on a water-cooled pulsed shearing process featuring reduced shear and suppressed heat accumulation. This strategy mitigates the transient coupling between mechanical forces and frictional heating during the DP, thereby constraining the energy input below the tolerance thresholds for carbon particle fracture and closed-pore carbon-iodine confinement failure, while maintaining it within the window between the PTFE fibrillation and fiber breakage (Scheme 1b). By employing micro-computed tomography (micro-CT), time-of-flight secondary ion mass spectrometry (TOF-SIMS), and other in/ex-situ spectral and structural characterizations, it demonstrates that the controlled shear force and the low-temperature assistance effectively suppress carbon particle damage and abnormal iodine migration, ensuring the consistent micro- to macro- scale binding of carbon-iodine, and guaranteeing the structural integrity and electrochemical stability of the thick iodine electrode. As a result, the iodine cathode delivers a reversible capacity of 214.3 mAh g^{-1} at 0.5 C, together with outstanding cycling stability over 50 000 cycles at 100 C. Furthermore, the iodine loading can be increased to 82.84 mg cm^{-2}, corresponding to an exceptional areal capacity of 16.27 mAh cm^{-2}. In pouch-cell demonstrations, a single-cell device retains a discharge capacity of 150.43 mAh g^{-1} after 1000 cycles at 2.5 C with a capacity retention of 96.23%. A 1.25 Ah pouch cell can be fabricated, exhibiting an average capacity decay of only 0.005% per cycle at 2 C. This study provides a new paradigm for fabricating ultrathick, high-loading iodine electrodes by regulating energy input during dry processing.

2 | Results and Discussion

2.1 | Multiscale Analysis and Precise Regulation of Abnormal Iodine Migration

To ensure a consistent initial state, iodine was first uniformly encapsulated within a porous active carbon (AC) matrix. Elemental mapping from transmission electron microscopy (TEM) images (Figure S1) clearly demonstrates the uniform distribution of iodine atoms within the porous AC matrix. The absence of crystalline I_2 peaks in the X-ray diffraction (XRD) patterns (Figure S2) indicates that iodine is present in a highly dispersed or amorphous state when confined within the AC pores [33, 34]. Nitrogen sorption measurements (Figure 1d; Figure S3) show a significant reduction in surface area from 1740.57 to 210.43 m^2 g^{-1} and in pore volume from 0.85 to 0.11 cm^3 g^{-1}, suggesting effective iodine encapsulation into the AC nanopores. Then AC@I_2, carbon nanotube (CNT), Super P, and PTFE were mixed through WP, high-shear dry processing (HS-DP), and low-temperature pulsed dry processing (LT-PDP) to fabricate electrodes (see Supporting Information for details).

As shown in Figure 1a, the excessive shear energy input in HS-DP induces severe mechanical collisions and friction, leading to carbon-iodine particle fragmentation and a markedly increased temperature rise rate. Raman spectra of both electrodes display two characteristic peaks centered at approximately 1350 and 1580 cm^{-1}, corresponding to the D and G bands of carbon, respectively, with the I_D/I_G ratio serving as an indicator of structural disorder (Figure 1b). Fitting calculation reveals that the signal of the HS-DP electrode at different positions fluctuates greatly, up to 1.02, which is associated with shear-induced defect generation and/or localized aggregation of conductive additives under excessive mechanical energy input. Thermogravimetric analysis (TGA, Figure 1c) of AC@I_2 based on different strategies reveals that the iodine retention in the LT-PDP reaches 50.18%, higher than HS-DP (48.71%) and WP (47.73%), highlighting its improved confinement effect. When the temperature exceeds ≈100°C, the WP electrode exhibits a sharp weight loss, suggesting the presence of free iodine that readily volatilizes (Figure S4). This stability arises from the reduced abnormal migration of iodine in the LT-PDP and minimized exposure of weakly bound free iodine. Consistent with this observation, Brunauer-Emmett-Teller (BET) analysis revealed that high shear treatment leads to a 55.5% increase in the specific surface area (327.30 m^2 g^{-1}), whereas the

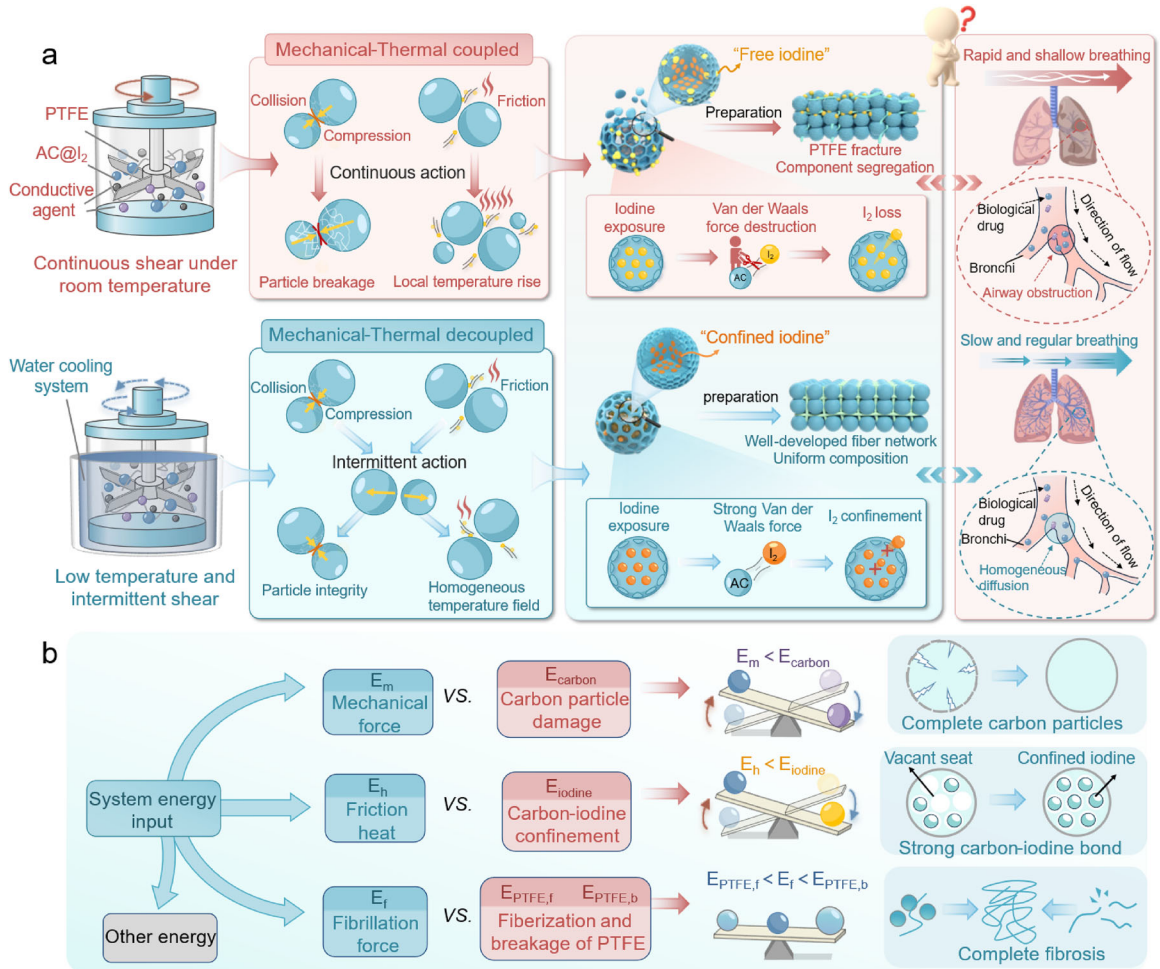

SCHEME 1 | Mechanical force-frictional heat decoupling engineering for thick iodine electrodes. (a) Diagram of the electrode failure mechanism under force-thermal coupling effects and the corresponding lung respiratory regulation mechanism. (b) Schematic of energy-threshold control.

LT-PDP/AC@I_2 shows a minimal increase of 2.3% compared with pristine AC@I_2 (Figure 1d). These behaviors can be attributed to the sustained action of high shear on the carbon framework, which induces irreversible fracture of low-crystallinity carbon, resulting in particle breakage, opening of originally closed pores at the micro–mesoscale, and the exposure of additional active sites.

Ultraviolet–visible (UV–vis) spectroscopy and iodine dissolution/adsorption experiments further demonstrate the superior iodine stability achieved by mechanical force-frictional heat decoupling engineering (Figure 1e,f). Compared with LT-PDP electrodes, HS-DP and WP electrodes exhibit deeper polyiodide color and stronger I_3^- absorption peak during the dissolution experiment. It can be attributed to the destruction of the pore structure, which leads to the extensive exposure of iodine originally confined within the carbon pores. This iodine transforms into "free iodine" and polyiodides. resulting in rapid dissolution and interface migration in the electrolyte (Figure 1g). To further assess the adsorption capacity of the host structures, three I_2-free electrodes fabricated via LT-PDP, HS-DP, and WP were immersed in polyiodide solution (Figure 1h,i). After 24 h, the solution containing the HS-DP electrode displays a slower color fading and intensified I_3^- absorption than LT-PDP, which can be attributed to weaker capture of iodine species caused by the destruction of mass transfer channels (Figure 1j). The WP solution also appeared nearly transparent, which can be attributed to residual solvent within the electrode and its loose structure containing considerable voids. These results demonstrate that the mechanical force-frictional heat decoupling regulation minimizes microstructural damage and preserves the initial confined carbon-iodine, thereby effectively reducing its dissolution [35].

2.2 | Multiscale Characterization of Electrode Structure and Properties

Apart from maintaining the energy input below the tolerance thresholds of carbon particle fracture and closed-pore iodine deconfinement, precisely stabilizing it within the PTFE fibrillation–fracture window is essential for achieving electrode robustness and component uniformity. The appropriate shear induces controlled deformation of PTFE, which then undergoes gradual fibrillation to form a continuous fiber network that effectively encapsulates the active materials and conductive agents. And the PTFE fibers will undergo excessive stretching or even breakage under high and continuous shear energy. Moreover,

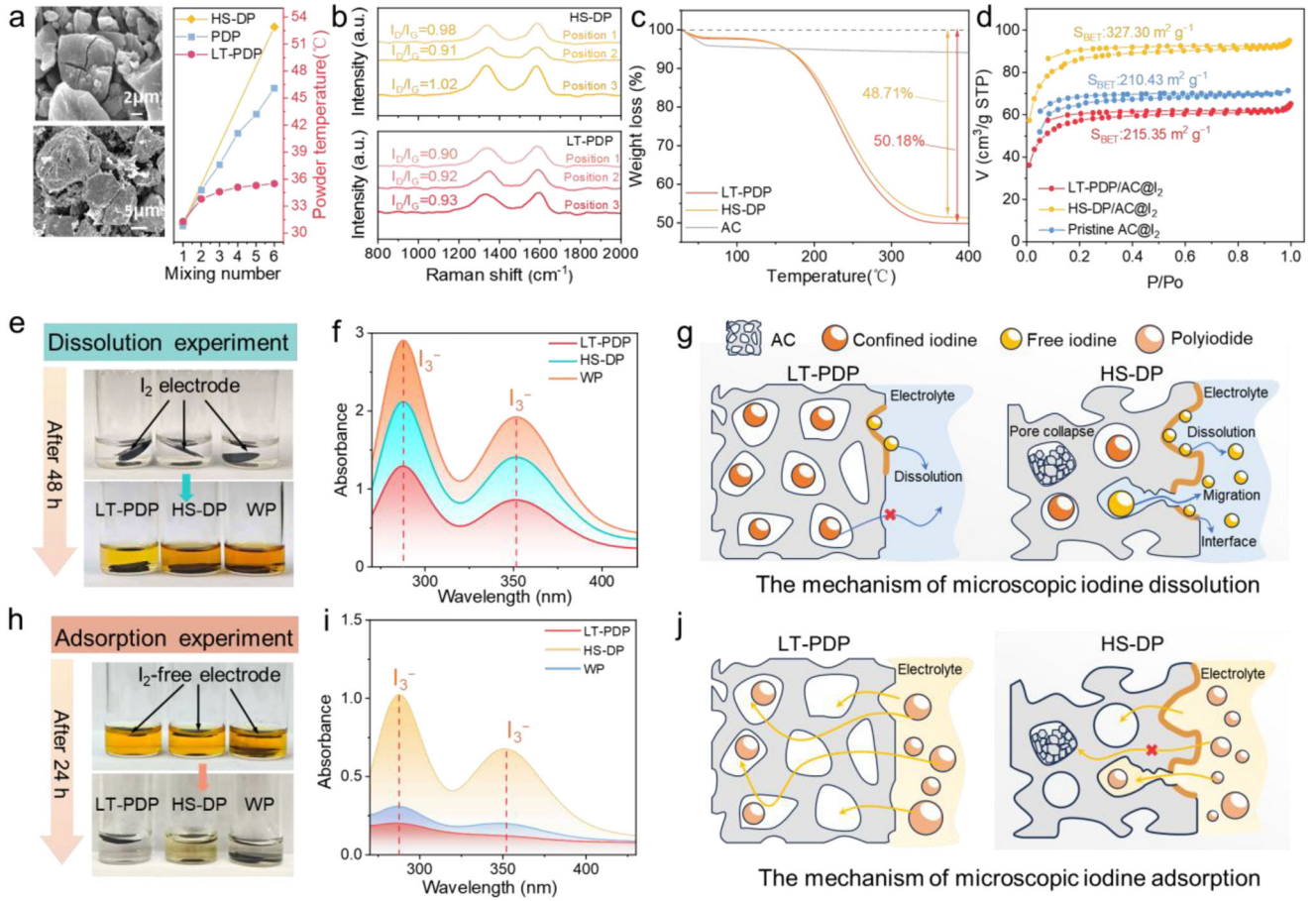

FIGURE 1 | Multiscale analysis and precise regulation of abnormal iodine migration. (a) SEM images of the surface of the HS-DP electrode (left) and temperature variations under different mixing conditions (right). (b) Comparison of Raman spectra of the LT-PDP and HS-DP electrodes at different positions. (c) TGA curves of the AC@I_2 based on HS-DP and LT-PDP strategies (d) Nitrogen isothermal absorption and desorption curves of the pristine AC@I_2, HS-DP/AC@I_2, and LT-PDP/AC@I_2 powder. (e) Optical images of the dissolution after 48 h for LT-PDP, HS-DP, and WP electrodes, and (f) corresponding UV–vis spectra. (g) The influence of changes in the carbon-iodine binding state. (h) Optical images of the absorption after 24 h for LT-PDP, HS-DP, and WP electrodes, and (i) corresponding UV–vis spectra. (j) The influence of mass transfer channels disruption.

different components experience uneven migration due to differences in particle size, density, and mechanical response, leading to component segregation and imbalanced spatial distribution.

Compared with the DP electrode, the WP electrode exhibits obvious iodine loss and structural disadvantages, including surface cracking, uneven particle and pore distribution, internal fissure and agent agglomeration (Figure 2a,d; Figure S5). Although both the HS-DP and LT-PDP electrodes exhibit relatively uniform component distribution in the 3D reconstructions of Micro-CT images (Figure 2b,c), localized regions of electrode collapse are observed in the HS-DP electrode cross-section. Quantitative analysis based on Micro-CT data reveals that the area fraction of large structural defects (equivalent diameter > 16 μm) is reduced from ≈2.4% in the HS-DP electrode to ≈0.8% in the LT-PDP electrode, indicating a substantially reduced degree of crack-related structural defects (Figure S6). Scanning electron microscopy (SEM) images at SEM 5000X further indicate the formation of a well-developed, entangled PTFE binder in the LT-PDP electrode, in sharp contrast to the disrupted fiber morphology in HS-DP (Figure 2e,f). This phenomenon originates from the accumulation of energy during continuous high shear mixing, resulting in PTFE fiber breakage and disruption of the "point-to-plane" binding network, thereby reducing mechanical strength and impairing electronic pathways. Mechanical tests validate these observations, namely, the obvious powder detachment after the wet electrode folding. The HS-DP electrode shows obvious surface cracks after two folding cycles. By contrast, the LT-PDP electrode tolerates folding without cracking or surface failure (Figure S7). Tensile tests show that in the initial elastic regime, LT-PDP exhibits a higher elastic modulus (0.034) than HS-DP (0.026), suggesting higher stiffness. Upon yielding, LT-PDP shows a discernible plastic deformation region. With increasing strain, the maximum elongation exceeds 2.4%, and the corresponding peak stress reaches approximately 0.037 MPa, indicating enhanced ductility compared to HS-DP (Figure 2g; Figure S8).

Particle size uniformity of the mixed composites was further evaluated with the equivalent area diameter defined as the diameter of a sphere having the same projected area as the particle (Figure S9). As shown in Figure 2h, the LT-PDP sample exhibits a highly concentrated size distribution dominated by particles in the 0–3 μm, whereas the HS-DP sample shows a broadened distribution spanning multiple size regimes, indicating the coexistence of particle fragmentation and shear-induced re-agglomeration under excessive energy input. As shown in Figure 2i, the

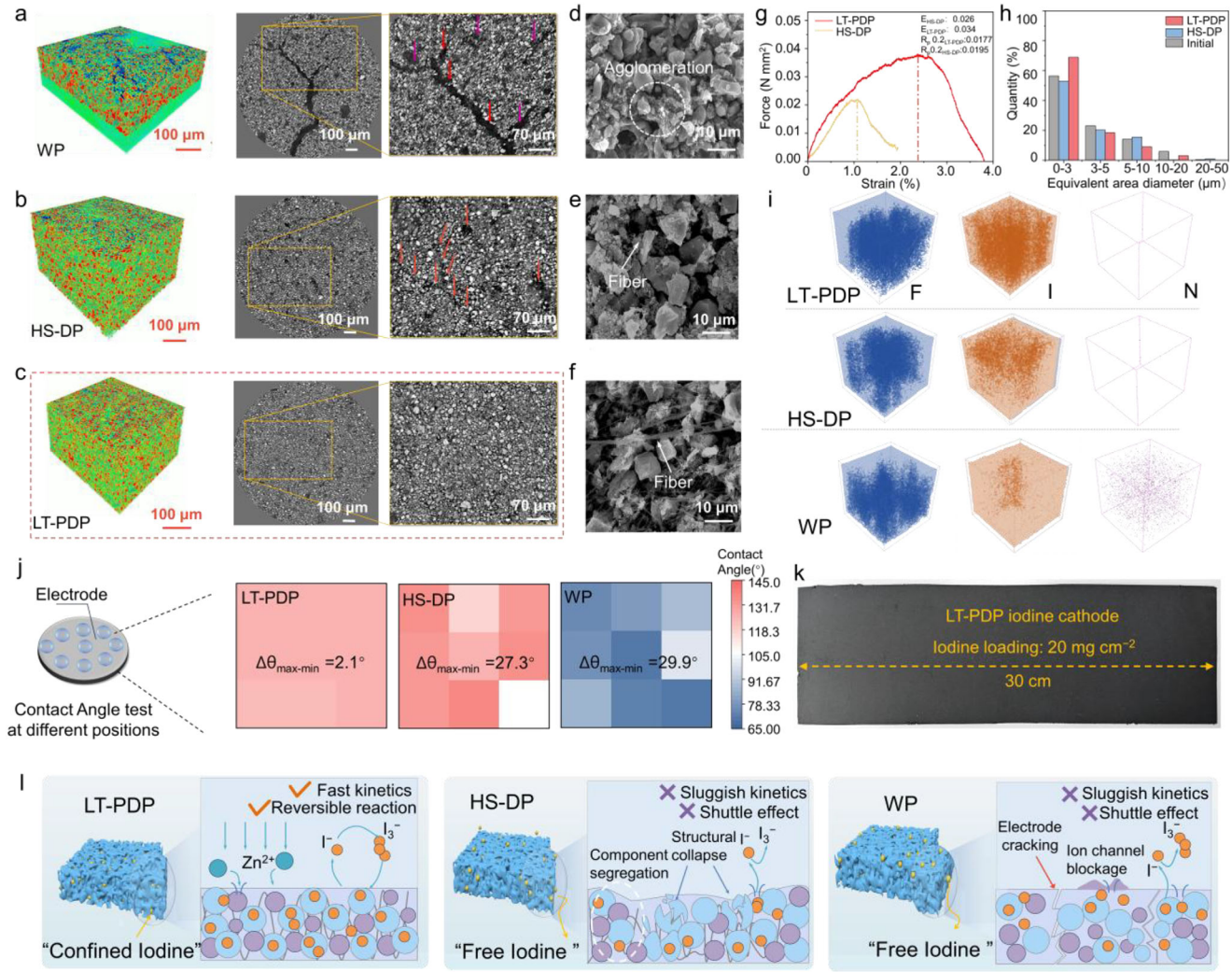

FIGURE 2 | Multiscale characterization of electrode structure and properties. Micro-CT 3D reconstructions and cross-sectional views of (a) WP, (b) HS-DP, and (c) LT-PDP electrodes (red: particles, blue-purple: pore). (d–f) SEM of three types of electrodes. (g) Tensile tests of LT-PDP and HS-DP electrodes (E: elasticity modulus; Rp0.2: 0.2% yield strength). (h) Particle size distribution expressed as area fraction versus equivalent diameter for the initial sample, HS-DP, and LT-PDP, obtained using a MixViewer 5000 system (M.I.P Technology, Changzhou, China). (i) TOF-SIMS of three types of electrodes. (j) The contact angles of the three electrodes at different positions. (k) The dry iodine electrode (20 mg cm^{-2}) extended to 30 cm. (l) Schematic illustration comparing the microstructure, iodine distribution, and resultant performance of electrodes fabricated via three processes.

distribution of iodine of the LT-PDP electrode remains highly uniform across various depths. By contrast, the WP electrode exhibits strong nitrogen (N) signal and weakened and irregular iodine (I) signal caused by solvent and thermal effects. Similarly, the HS-DP electrode also exhibits an uneven iodine distribution, which can be attributed to abnormal migration of iodine caused by local temperature rise.

This structural uniformity is further reflected in the wetting behavior of the electrode surface (Figure 2j; Figure S10). The WP electrode exhibits a lower average contact angle but large regions of fluctuations (29.9°) owing to residual polar solvents and surface defects. The HS-DP electrode shows a larger contact angle and region variations (27.3°), arising from the weak ability to bond with water and localized surface defects. In contrast, the LT-PDP electrode exhibits a highly consistent contact angle, with a minimal variation of only 2.1°, indicating a well-defined and homogeneous interfacial structure. Correspondingly, electrochemical impedance spectroscopy (EIS) reveals that the LT-PDP electrode possesses the lowest fitted charge transfer resistance (R_{ct} = 72.7 Ω) compared with the WP (93 Ω) and the HS-DP (101 Ω), suggesting a desirable electrode interface state (Figure S11). Based on these features, the LT-PDP enables the construction of thick electrodes with steadily increasing iodine loading up to ≈50 mg cm^{-2}, while maintaining dense and structurally intact (Figures S12 and S13). Importantly, benefiting from its scalable and controllable fabrication process, the length of the resulting flexible electrode can be extended to 30 cm, demonstrating potential for roll-to-roll production at a meter scale (Figure 2k).

The above experimental observations indicate that the LT-PDP electrode exhibits enhanced structural consistency and compositional homogeneity. Against this background, a COMSOL Multiphysics model parameterized by experimentally derived inputs was employed to qualitatively compare the coupled transport and reaction behavior of electrodes fabricated via different

processing routes. The simulation results indicate that, under identical boundary conditions, the LT-PDP electrode displays faster and more spatially uniform zincation behavior (Figure S14a). Correspondingly, the electrolyte transport distributions in the idealized model (Figure S14b) reveal relatively more coherent transport features in the LT-PDP electrode, whereas the WP electrode is characterized by more tortuous and discontinuous pathways, highlighting differences in transport and reaction coupling associated with microstructural variations. Taken together, the structural integrity and effective iodine confinement maintained by the water-cooled pulsed shear processing facilitate a more homogeneous reaction environment, mitigate localized accumulation of polyiodide species, and are associated with more stable reaction kinetics and cycling performance in subsequent electrochemical evaluations (Figure 2l).

2.3 | Electrochemical Mechanism of Electrode Configurations

I_2 acts as an active cathode material and undergoes a reversible I_2/I^- redox reaction ($I_2 + 2e^- \rightleftharpoons 2I^-$). During this process, polyiodide species may form as transient intermediates. In situ UV–vis absorption spectroscopy was conducted using a quartz as the reaction vessel in an open-cell configuration (Figure 3a; Figure S15). The images indicate that while the HS-DP and WP electrodes exhibit a pronounced increase in I_3^- absorbance during charging, the LT-PDP electrode maintains a consistently low intensity (Figure 3b). In situ Raman presents the signals of I_3^- (≈105 cm^{-1}) and I_5^- (≈163 cm^{-1}) intermediates during the I^-/I° conversion. The WP electrode exhibits intense and uneven I_2/I_3^- transitions, indicating unavoidable polyiodide local aggregation and shuttling. In sharp contrast to the WP, the LT-PDP electrode exhibits only weak I_3^-/I_5^- signals, implying that the polyiodide dissolution and migration are effectively suppressed (Figure 3e,f). These results demonstrate that the 3D confined network constructed by the LT-PDP effectively stabilizes iodine species, mitigates excessive polyiodide dissolution and shuttling, and ensures a more uniform and controllable I_2/I^- conversion process [36].

Gas evolution measurements further highlight the stability advantage of the LT-PDP electrode (Figure 3c). With increasing time, the gas production rate of the LT-PDP electrode decreases. After 7 h of cycling, the accumulated gas volumes of the WP and HS-DP electrodes reached 28.73 µL and 25.23 µL, respectively, whereas the LT-PDP electrode produced only 19.14 µL (Figure 3d; Figure S16). This reduction is closely associated with suppressed I_3^- migration, which otherwise induces overcharging, decreases the Coulombic efficiency (CE), and triggers severe self-discharge during rest. As shown in Figure 3g, the LT-PDP cell demonstrates significantly improved stability: At 100% state of charge (SOC), the LT-PDP cell exhibits only 4.6% capacity decay after resting for 48 h, compared with 11.4% for the WP cell and 5.5% for the HS-DP cell. These results underscore the effectiveness of the 3D porous framework constructed via the LT-PDP in mitigating the shuttle effect [37].

As the anode, zinc undergoes reversible dissolution and deposition ($Zn \rightleftharpoons Zn^{2+} + 2e^-$). The migration of polyiodide to their surface triggers the side reaction, disrupting the local redox balance and consequently inducing a series of electrode interface issues. As shown in XRD patterns (Figure 3h), a diffraction peak at approximately 8.5° corresponding to $Zn_4SO_4(OH)_6{\bullet}4H_2O$ formation (JCPDS No. 44–0673) is clearly observed on the anodes cycled in Zn-I_2 cells with the WP and HS-DP cathodes [38]. In contrast, the by-product peak is nearly absent on the Zn anode paired with the LT-PDP cathode, indicating that the anode-side reactions are effectively mitigated [39–41]. In XPS, S 2p characteristic peaks were detected in the range of 167–172 eV and 158–165 eV, corresponding to the existence of S—O and Zn—S bonds after 50 cycles. Under HS-DP and WP conditions, sulfur-containing species such as Zn—S, SO_4^{2-}, and SO_3^{2-} accumulated significantly, indicating frequent side reactions. Meanwhile, the Zn^{2+} signal in the Zn 2p spectrum of cycled Zn metal with the LT-PDP as cathode decreased, indicating fewer Zn/O-related by-products on the electrode surface. Additionally, in the batteries using WP and HS-DP cathodes, XPS analysis of the Zn metal surface showed a stronger I 3d peak, indicating the presence of abundant polyiodide species and further confirming iodine shuttle behavior (Figure S17). Confocal laser scanning microscopy (CLSM) and SEM analysis revealed obvious dendrites and by-products on the Zn anode surface when paired with HS-DP and WP cathodes after cycling, resulting from uneven zinc deposition and severe side reactions (Figure 3i; Figure S18). In contrast, the Zn surface when paired with the LT-PDP cathode remains smooth and flat, with no detectable zinc dendrites. It is clear that the polyiodide shuttles to the anode along a concentration gradient and triggers Zn corrosion, thereby resulting in active material loss and battery performance decay (Figure 3j) [42, 43]. Based on these results, the electrode structure constructed via low-temperature pulse shearing, combined with spatial confinement of iodine, accelerates iodine conversion rate, prevents polyiodide accumulation and shuttling, suppresses the polyiodide-induced corrosion and parasitic reactions on the zinc anode, and thereby enables ultra-stable, long-life, and non-shuttling Zn–I_2 batteries.

2.4 | Electrochemical Characterization of the Zn–I_2 Coin Cells

The LT-PDP electrode provides efficient Zn^{2+} transport channels with enhanced transfer kinetics. The cyclic voltammetry curves at 0.1 mV s^{-1} show that the LT-PDP electrode exhibits a higher peak current and a smaller peak voltage difference than the HS-DP and WP electrodes, indicating faster transfer and better reversibility (Figure S19) [44]. With the increase of scan rate from 0.2 to 1.0 mV s^{-1}, the linear relationship between the peak current and scan rate and fitted *b*-values (0.80/0.74) indicate that the redox kinetics are governed by a combination of surface capacitive behavior and ion diffusion. Notably, the LT-PDP electrode consistently delivered an 83.9% capacitive contribution at 1.0 mV s^{-1}, significantly higher than that of HS-DP (76.1%) and WP (70.4%). This suggests that fast surface reactions of the LT-PDP electrode dominate under high-rate conditions, thereby alleviating reliance on long-range ion diffusion (Figure S20). The apparent diffusion coefficient of the LT-PDP electrode fitted from the Galvanostatic Intermittent Titration Technique was between 10^{-5} and 10^{-6}, which was up to ≈10 times higher than that of WP electrode (Figure S21). The network structure of LT-PDP facilitates rapid Zn^{2+} transport, endowing improved rate performance. Compared with the other two electrodes, the LT-PDP electrode exhibits higher

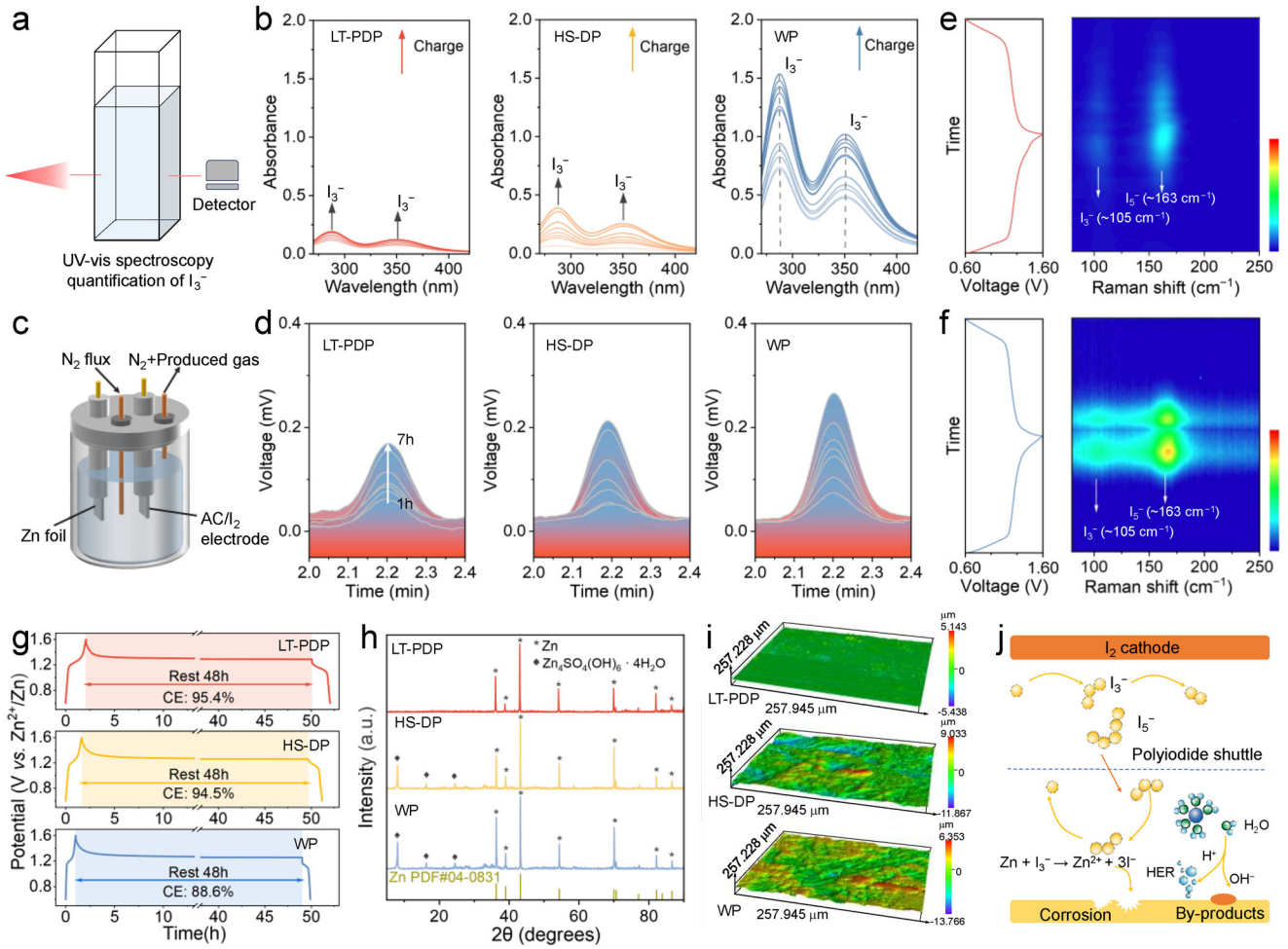

FIGURE 3 | Analysis of polyiodide shuttling behavior of thick iodine electrodes and morphology and surface characterization of zinc anodes. (a) Schematic diagram of in situ UV-Vis test device. (b) In situ UV-Vis spectra. (c) Gas testing device. (d) The amount of gas produced by the three electrodes increases over time. (e,f) In situ Raman of LT-PDP and WP electrodes. (g) Battery self-discharge test. (h) XRD patterns and (i) CLSM images of Zn anodes after cycling in Zn-I_2 cells with the three cathodes. (j) The challenge posed by the polyiodide shuttling to the Zn anode.

specific capacity and battery CE at different current densities (Figure 4a,b). At a high rate of 50 C, the LT-PDP electrode battery delivers a reversible capacity of 128.62 mAh g^{-1} with 98.3% capacity retention after 12000 cycles, which was superior to that of the HS-DP and WP (Figure S22).

In addition to its favorable rate capability, the cycle stability of the LT-PDP electrode was evaluated under the mass loading of iodine lower than 10 mg cm^{-2}. As shown in Figure 4c, the WP electrode exhibits low initial capacity (106.1 mAh g^{-1}) and poor retention (78.39% after 1000 cycles). HS-DP electrode shows improved capacity (≈200 mAh g^{-1}) but rapid fading to 161.3 mAh g^{-1} after 700 cycles. In striking contrast, an initial specific capacity of 214.3 mAh g^{-1} is delivered by the LT-PDP electrode with 94.37% retention over 1000 cycles. The GCD curve further demonstrates that the Zn-I_2 battery prepared by the LT-PDP electrode exhibit less capacity attenuation during long-term cycling, indicating that the spatial regulation of iodine by the pulse dry mixing not only helps suppress the shuttle effect but also facilitate the rapid conversion kinetics of iodine (Figure S23). Even with an extremely high rate of 100 C, the LT-PDP electrode delivers an extremely long cycle life of over 50 000 times, with a capacity retention rate of 92.74% (Figure 4d). The battery performance based on LT-PDP cathode surpasses most previously reported Zn-I_2 batteries in terms of capacity retention and cycle life (Figure 4e and Table S1) [3, 7, 20, 45].

The LT-PDP electrode also delivers exceptional areal performance across a wide range of iodine loading. As the loading increased from 20.95 to 47.15 mg cm^{-2}, the specific capacity at 0.25 C remained stable, and the corresponding areal capacities increased steadily to 4.78, 5.59, 6.69, and 9.13 mAh cm^{-2} (Figure 4f). Even under the ultra-high load of 82.84 mg cm^{-2}, the displayed area capacity reached 16.27 mAh cm^{-2}, indicating remarkable structural integrity and reaction uniformity (Figure S24). Furthermore, the cell retained a high areal capacity of 8.6 mAh cm^{-2} after 750 cycles at a rate of 1 C with an iodine loading of 51.25 mg cm^{-2} (Figure 4g). These results further corroborate that the highly uniform, confined network constructed via the LT-PDP enables efficient ion transport and robust redox kinetics, even under ultrahigh iodine loading conditions. The combination of ultrahigh iodine loading and high specific capacity leads to a superior areal capacity, exceeding that of the previously reported Zn–I_2 battery (Figure 4h) [7, 46–51].

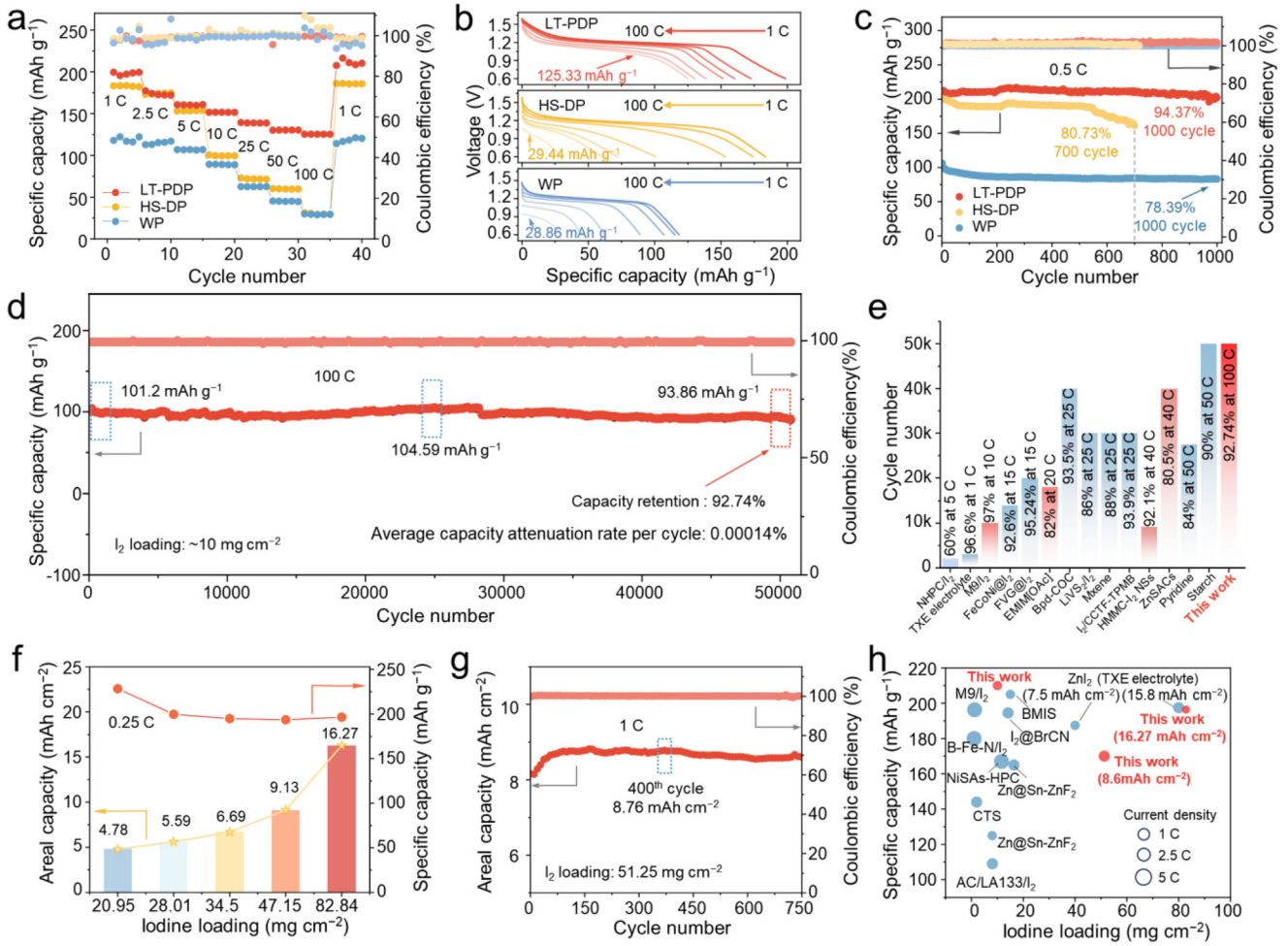

FIGURE 4 | Electrochemical performance of Zn–I_2 coin cells. (a) Rate capability comparison. (b) Discharge curves of the battery at different current densities. Cycling performance of the electrodes at (c) 0.5 C and (d) 100 C. (e) Cycle performance and capacity retention of different batteries. (f) Areal capacity under different iodine mass loadings at 0.25 C. (g) Battery cycling performance under high mass loading at 1 C. (h) Battery performance comparison.

2.5 | Ah-Level Pouch Cell Evaluation and Application Demonstration

To further explore the practical value of the LT-PDP in high-specific-energy Zn–I_2 batteries, a series of high-loading pouch cells was assembled. The Zn-I_2 pouch cell with the iodine loading up to 15 mg cm^{-2} maintained a capacity retention rate of 96.23% after 1000 cycles at 2.5 C, demonstrating outstanding cycling stability (Figure 5a). The inset images further illustrate that the pouch cell displayed a stable voltage under destructive tests, including heating, needling, and bending. When the current density was further increased to 10 C, the battery capacity could still retain a capacity of 124.6 mAh g^{-1} (Figure S25). These results of self-discharge test show that the capacity retention rate of the pouch cell after resting 48 h is as high as 97.7%, which can be attributed to the effective confinement of active iodine species and the reduction of free iodine, thereby suppressing the polyiodide shuttle (Figure 5b).

In addition, we have successfully fabricated a pouch cell using 90 × 100 mm cathodes via electrode lamination technology (Figure S26). Under the more demanding condition of an iodine loading of 31 mg cm^{-2}, the capacity can reach up to 1.25 Ah, and an average capacity decay of only 0.005% per cycle at 2 C, further highlighting the scalability of this strategy (Figure 5c). Notably, the overall performance outperforms most previously reported Zn–I_2 aqueous systems (Table S2). The proposed fabrication process ensures good consistency of the pouch cells, enabling their assembly in series with stable performance. The assembled pouch cell pack delivers a stable output voltage of 3.4 V after combining and can serve as a power source for a toy car (Figure 5d and Video S1). These results indicate that the LT-PDP not only enhances the electrochemical performance of the battery but also provides a feasible solution for the large-scale application of zinc-iodine aqueous batteries through the mechanical support of the fiber network and interface optimization.

3 | Conclusion

In this work, we systematically analyze the failure mechanism of the electrode structure and interface caused by the

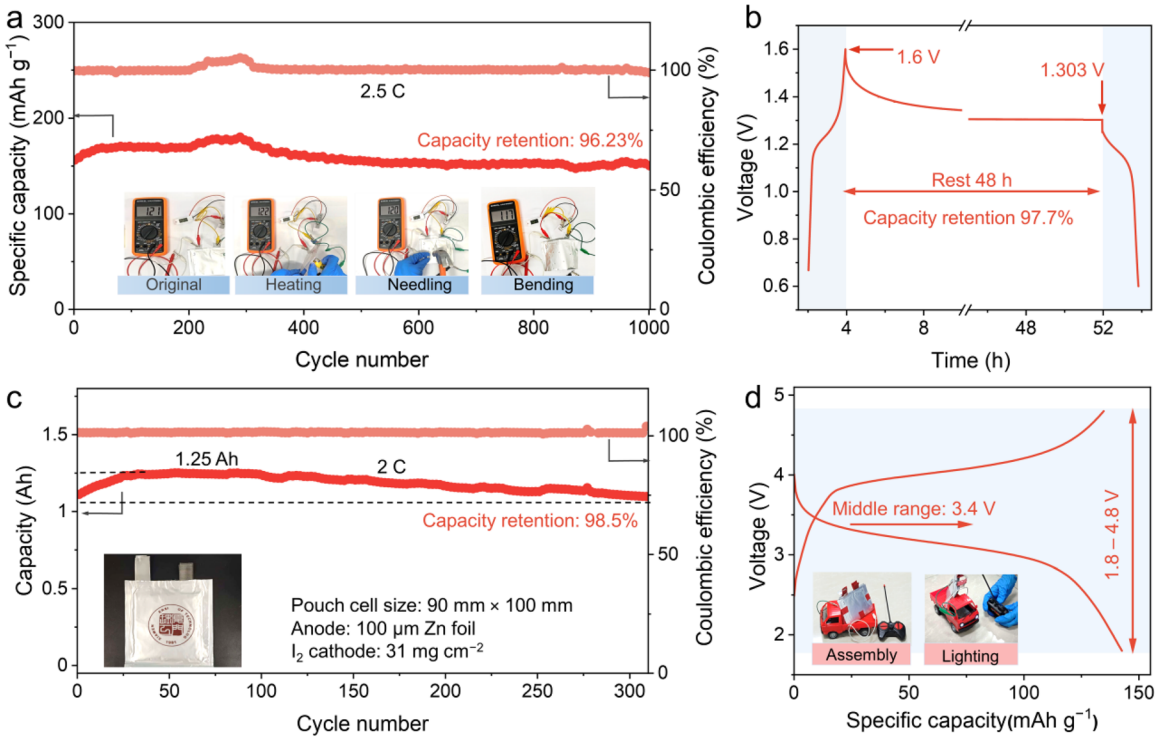

FIGURE 5 | Electrochemical performance of Zn–I_2 pouch cells. (a) Cycling performance of a single-cell pouch battery at a high rate of 2.5 C (Insets: photographs of destructive tests under extreme conditions). (b) Self-discharge of the pouch cell. (c) Cycling performance of Ah-level pouch battery with high-loading iodine cathode of 31 mg cm^{-2}. (d) GCD curve of series pouch cells (Insets: photographs of the pouch cells powering a toy car).

uncontrolled mechanical-thermal coupling effect under continuous shearing. A targeted energy intermittent release strategy based on a low-temperature environment was employed to achieve precise decoupling and regulation of the mechanical force and frictional heat accumulation. This strategy reduced carbon host structure damage and carbon-iodine deconfinement, thereby fundamentally inhibiting the transition of iodine from a confined state within active carbon pores to free iodine that is susceptible to migration and loss. The resulting electrode possesses a robust 3D network that ensures uniform charge transport pathways. As a result, the LT-PDP electrode delivers a reversible capacity of 214.3 mAh g^{-1} under a high areal loading of ≈10 mg cm^{-2} at 0.5 C, and demonstrates extraordinary cycling stability with 92.74% capacity retention after 50000 cycles at an ultrahigh rate of 100 C. By increasing the electrode thickness, the iodine loading is further elevated to 82.84 mg cm^{-2}, achieving an exceptional areal capacity of 16.27 mAh cm^{-2}. Furthermore, a 1.25 Ah-level pouch cell is successfully assembled with an average capacity decay of only 0.005% per cycle at 2 C under high-loading conditions. This study breaks through the traditional perception that solvent-free dry processes yield no iodine loss, providing a novel and effective fabrication strategy for achieving optimal iodine confinement in thick electrodes.

Acknowledgements

This work was supported by the National Natural Science Foundation of China (Nos. 22509170, U24A2060, and 22279023), the Natural Science Foundation of Fujian Province (No. 2024J011210), the Fundamental Research Funds for the Central Universities (No. 20720250005), Science and Technology Commission of Shanghai Municipality (Nos. 25DZ3002901, 2024ZDSYS02, 25PY2600100), China Postdoctoral Science Foundation (No. 2022TQ0282), the High-Level Talent Start-Up Foundation of Xiamen Institute of Technology for financial support (No. YKJ23017R) and the 2024 Xiamen Institute of Technology Training Foundation (No. XPYQ2403). The authors thank the AI for Science Foundation of Fudan University (FudanX24A1035), and Shanghai Pilot Program for Basic Research—Fudan University 21TQ1400100 (25TQ012). The authors extend their gratitude to Ms. Sun Jiawen for providing invaluable assistance with the BET analysis and Olegeeino (Chongqing) New Materials Co., Ltd. for providing the experimental materials.

Conflicts of Interest

The authors declare no conflicts of interest.

Data Availability Statement

The data that supports the findings of this study are available in the supplementary material of this article

References

1. C. X. Dong, Y. K. Yu, C. N. Ma, et al., "Tailoring Zinc Diatomic Bidirectional Catalysts Achieving Orbital Coupling–Hybridization for Ultralong-Cycling Zinc–Iodine Batteries," *Energy & Environmental Science* 18 (2025): 3014–3025, https://doi.org/10.1039/D4EE05767H.

2. H. Luo, X. Su, Z. Chen, et al., "Aqueous Iron-Ions Batteries: Status, Solutions, and Prospects," *Advanced Materials* 37 (2025): 2507978, https://doi.org/10.1002/adma.202507978.

3. W. Yan, Y. Liu, J. Qiu, et al., "A Tripartite Synergistic Optimization Strategy for Zinc-Iodine Batteries," *Nature Communications* 15 (2024): 9702, https://doi.org/10.1038/s41467-024-53800-6.

4. P. Hei, Y. Sai, W. Li, et al., "Diatomic Catalysts for Aqueous Zinc-Iodine Batteries: Mechanistic Insights and Design Strategies," *Angewandte Chemie International Edition* 63 (2024): 202410848, https://doi.org/10.1002/anie.202410848.

5. H. Luo, H. Guo, X. Li, et al., "Aqueous manganese-ion batteries: The past, present, and future," *Matter* 8 (2025): 102379, https://doi.org/10.1016/j.matt.2025.102379.

6. Q. Chen, J. Hao, Y. Zhu, et al., "Anti-Swelling Microporous Membrane for High-Capacity and Long-Life Zn—I_2 Batteries," *Angewandte Chemie International Edition* 64 (2025): e202413703, https://doi.org/10.1002/anie.202413703.

7. H. Wu, S.-J. Zhang, J. Vongsvivut, M. Jaroniec, J. Hao, and S.-Z. Qiao, "Aqueous Zinc-Iodine Batteries With Ultra-High Loading and Advanced Performance," *Joule* 9 (2025): 102000, https://doi.org/10.1016/j.joule.2025.102000.

8. Q. Yu, X. Zhang, D. Yuan, et al., "A Gradient Functionalized Separator for Unlocking Latent Cathode Host Sites and Enhancing Zinc Anode DOD in Ultrahigh-Areal-Capacity Static Zn-I_2 Batteries" *Advanced Materials* 38 (2026): e23132, https://doi.org/10.1002/adma.202523132.

9. X. Cui, L. Liu, X. Li, et al., "Dual-pathway proton transport blockade enabling high areal loading aqueous zinc metal batteries," *Energy & Environmental Science* 19 (2025): 1006, http://dx.doi.org/10.1039/D5EE06001J.

10. Y. Li, H. Luo, S. Yang, et al., "An Ultra-Thick Solvent-Free Electrode Based on Non-Conservative Pulsed Shear Field Mixing," *Energy Storage Materials* 77 (2025): 104218, https://doi.org/10.1016/j.ensm.2025.104218.

11. L. Zhou, G. Zhang, J. Guo, et al., "Electrostatic–Immobilized Polyiodides via Bifunctional Quaternary Ammonium Binder for Shuttle–Free and Ultra–Stable Zn–I_2 Batteries," *Advanced Functional Materials* 35 (2025): e13527, https://doi.org/10.1002/adfm.202513527.

12. T. Liu, Y. Sun, Y. Wang, et al., "Architected continuum mixed ionic and electronic conducting alloy negative electrode for fast-charging all-solid-state lithium batteries", *Nature Communications* 17 (2026): 706, https://doi.org/10.1038/s41467-025-67352-w.

13. Y. Y. Wang, H. Chen, J.-L. Yang, et al., "Flexible, Stackable, and Fully Active Thick Electrode with Scalable 3D Topology Braid Structure Enables Supercontinuous Electron/Ion Transport", *Advanced Materials* 38 (2026): e15575, https://doi.org/10.1002/adma.202515575.

14. J. Wu, H. Guo, R. Wang, et al., "Fabrication of low-tortuosity thick electrodes with low material loss by temporally shaped ultraviolet femtosecond laser", *Nature Communications* 17 (2025): 973, https://doi.org/10.1038/s41467-025-67702-8.

15. L. Chen, S. Huang, Z. Feng, et al., "Local Electric Field Microenvironment-Induced Dynamic Confinement to Stabilize I^+ Toward High-Mass-Loading and Stable Zinc-Iodine Batteries," *Angewandte Chemie International Edition* 64 (2025): e202510737, https://doi.org/10.1002/anie.202510737.

16. M. Chen, H. Li, H. Xu, et al., "Redirecting iodine reduction pathways by decoupling adsorption energies for long-life Zn–I_2 batteries," *Energy & Environmental Science* 19 (2025): 896, http://dx.doi.org/10.1039/D5EE06963G.

17. S.-J. Zhang, J. Hao, H. Wu, et al., "Coordination Chemistry toward Advanced Zn–I_2 Batteries with Four-Electron I–/I^0/I^+ Conversion," *Journal of the American Chemical Society* 147 (2025): 16350, https://doi.org/10.1021/jacs.5c02085.

18. H. Luo, F. Li, M. Wang, et al., "Reconstructing the Phase of Vanadium Oxides Enables Redox-Catalysis Manipulated Reversible Sulfur Conversion For Stable Zn–S Batteries," *Chemical Science* 16 (2025): 753–760, https://doi.org/10.1039/D4SC06593J.

19. Y. Tan, W. Xu, F. Yang, et al., "Dynamic Polyiodide-Trapping and Proton-Capturing Dual-Network Engineering for High-Areal-Capacity, Long-Cycling and High-Temperature Zn—I_2 Batteries," *Advanced Materials* 38 (2026): 22609, https://doi.org/10.1002/adma.202522609.

20. F. Li, S. Sun, L. Ma, et al., "Iron-Regulated D-Band Center in Fe-V_2O_5-n/rGO for Enhanced Electrocatalytic Performance," *Advanced Functional Materials* 36 (2026): e12876, https://doi.org/10.1002/adfm.202512876.

21. T. Zhang, Z. Qin, X. Long, et al., "Stable Molten Salts Mediated Growth of Single-Crystalline $LiNi_{0.8}$ $Co_{0.1}$ $Mn_{0.1}$ O_2 With High Voltage Tolerance," *Advanced Functional Materials* 35 (2025): 2500608, https://doi.org/10.1002/adfm.202500608.

22. W. Zeng, F. Xia, J. Wang, et al., "Entropy-Increased $LiMn_2O_4$-Based Positive Electrodes for Fast-Charging Lithium Metal Batteries," *Nature Communications* 15 (2024): 7371, https://doi.org/10.1038/s41467-024-51168-1.

23. S. Li, Y. Nie, Y. Wang, et al., "Quantum Size Effect Synergizes Space-Limited Domain Action for Advanced Aqueous Zinc-Iodine Batteries," *Advanced Materials* 37 (2025): 14577, https://doi.org/10.1002/adma.202514577.

24. R. Yuan, Y. Dong, R. Hou, et al., "Structural Transformation of Porous and Disordered Carbon During Ball-Milling," *Chemical Engineering Journal* 454 (2023): 140418, https://doi.org/10.1016/j.cej.2022.140418.

25. Z. Zhao, H. Chen, W. Zhang, et al., "Defect Engineering in Carbon Materials for Electrochemical Energy Storage and Catalytic Conversion," *Materials Advances* 4 (2023): 835–867, https://doi.org/10.1039/D2MA01009G.

26. K. Ganesan, R. Rani, T. Mathews, and S. Dhara, "Direct Microscopic Evidence of Shear Induced Graphitization of Ultrananocrystalline Diamond Films," *Carbon Trends* 4 (2021): 100078, https://doi.org/10.1016/j.cartre.2021.100078.

27. B. Qi, Y. Chai, Y. Hu, et al., "Confinement of Polyiodides by Dual-Functional Tetrazine Cathodes in Zn–I_2 Batteries," *Angewandte Chemie International Edition* 64 (2025): 202507497, https://doi.org/10.1002/anie.202507497.

28. J. Hu, Z. Zhang, T. Deng, et al., "Porous Aromatic Frameworks Enabling Polyiodide Confinement Toward High Capacity and Long Lifespan Zinc–Iodine Batteries," *Advanced Materials* 36 (2024): 2401091, https://doi.org/10.1002/adma.202401091.

29. X. Chang and A. Cabot, "Insights on Polyidide Shuttling of Zn-I_2 Batteries by I_3^-/I^- Electrolytes Based on the Dual-Ion Battery System," *Nanomaterials* 15 (2025): 738, https://doi.org/10.3390/nano15100738.

30. J. Xu, Z. Huang, H. Zhou, G. He, Y. Zhao, and H. Li, "Holistic Optimization Strategies for Advanced Aqueous Zinc Iodine Batteries," *Energy Storage Materials* 72 (2024): 103596, https://doi.org/10.1016/j.ensm.2024.103596.

31. S. Yang, C. Li, H. Lv, et al., "High-Rate Aqueous Aluminum-Ion Batteries Enabled by Confined Iodine Conversion Chemistry," *Small Methods* 5 (2021): 2100611, https://doi.org/10.1002/smtd.202100611.

32. K. Sugano, Y. Uchida, O. Ichihashi, H. Yamada, T. Tsuchiya, and O. Tabata, "Mixing Speed-Controlled Gold Nanoparticle Synthesis With Pulsed Mixing Microfluidic System," *Microfluidics and Nanofluidics* 9 (2010): 1165–1174, https://doi.org/10.1007/s10404-010-0637-9.

33. F. Li, C. Zhou, J. Zhang, et al., "Mullite Mineral-Derived Robust Solid Electrolyte Enables Polyiodide Shuttle-Free Zinc-Iodine Batteries," *Advanced Materials* 36 (2024): 2408213, https://doi.org/10.1002/adma.202408213.

34. H. Sun, M. Li, J. Zhu, J. Ni, and L. Li, "Capitalizing on the Iodometric Reaction for Energetic Aqueous Energy Storage," *ACS Nano* 18 (2024): 21472–21479, https://doi.org/10.1021/acsnano.4c06252.

35. S. J. Zhang, J. Hao, H. Wu, Q. Chen, C. Ye, and S. Z. Qiao, "Protein Interfacial Gelation Toward Shuttle-Free and Dendrite-Free Zn–Iodine Batteries," *Advanced Materials* 36 (2024): 2404011, https://doi.org/10.1002/adma.202404011.

36. L. Tan, J. Wei, L. Xue, et al., "Regulating the Electron Structure of Covalent Organic Frameworks to Enable Excellent Cycle Life and High Rate Toward Advanced Zn—I_2 Batteries," *Advanced Functional Materials* 35 (2025): 2416931, https://doi.org/10.1002/adfm.202416931.

37. L. Li, R. Bu, W. Zhong, et al., "Densely Packed and Vertically Oriented Covalent Organic Framework Membrane Enabled Efficient Ion Sieving for Zinc Iodine Battery," *Nano Energy* 138 (2025): 110886, https://doi.org/10.1016/j.nanoen.2025.110886.

38. S. J. Zhang, J. Hao, D. Luo, et al., "Dual-Function Electrolyte Additive for Highly Reversible Zn Anode," *Advanced Energy Materials* 11 (2021): 2102010, https://doi.org/10.1002/aenm.202102010.

39. J. Hao, B. Li, X. Li, et al., "An In-Depth Study of Zn Metal Surface Chemistry for Advanced Aqueous Zn-Ion Batteries," *Advanced Materials* 32 (2020): 2003021, https://doi.org/10.1002/adma.202003021.

40. J. Bu, P. Liu, G. Ou, et al., "Interfacial Adsorption Layers Based on Amino Acid Analogues to Enable Dual Stabilization Toward Long-Life Aqueous Zinc Iodine Batteries," *Advanced Materials* 37 (2025): 2420221, https://doi.org/10.1002/adma.202420221.

41. X. Su, S. Li, Z. Chen, et al., "Steering Zn(ClO4)2 Electrolyte: Trifunctional Polycationic Artificial Interphase for Wide-Temperature Ah-level Zn-I2 Pouch Cells," *Energy Storage Materials* 85 (2026): 104900, https://doi.org/10.1016/j.ensm.2026.104900.

42. Y. Wang, Y. Lv, S. Wei, et al., "Polymerized Melamine Catalyzes Direct I^- /I_2 Conversion via —N═N— Motif for High Capacity Zn-I_2 Batteries," *Advanced Materials* 38 (2026): 15000, https://doi.org/10.1002/adma.202515000.

43. W. Gao, S. Cheng, Y. Zhang, E. Xie, and J. Fu, "Efficient Charge Storage in Zinc–Iodine Batteries based on Pre-Embedded Iodine-Ions with Reduced Electrochemical Reaction Barrier and Suppression of Polyiodide Self-Shuttle Effect," *Advanced Functional Materials* 33 (2023): 2211979, https://doi.org/10.1002/adfm.202211979.

44. Z. Feng, Y. Tang, Y. Wei, et al., "Reducing Dead Species by Electrochemically-Densified Cathode-Interface-Reaction Layer towards High-Rate-Endurable Zn||I-Br Batteries," *Angewandte Chemie International Edition* 64 (2025): 202416755, https://doi.org/10.1002/anie.202416755.

45. Y. Zhao, Y. Wang, W. Xue, et al., "Elucidating Synergistic Mechanism of Zinc Single-Atom Sites and Lewis Acid–Base Pairs to Boost Zinc–Iodine Batteries Performance," *Advanced Functional Materials* 35 (2025): 2422677, https://doi.org/10.1002/adfm.202422677.

46. H. Wu, J. Hao, S. Zhang, et al., "Aqueous Zinc–Iodine Pouch Cells With Long Cycling Life and Low Self-Discharge," *Journal of the American Chemical Society* 146 (2024): 16601–16608, https://doi.org/10.1021/jacs.4c03518.

47. J. Ma, A. Azizi, E. Zhang, H. Zhang, A. Pan, and K. Lu, "Unleashing the High Energy Potential of Zinc–Iodide Batteries: High-Loaded Thick Electrodes Designed With Zinc iodide as the cathode," *Chemical Science* 15 (2024): 4581–4589, https://doi.org/10.1039/D4SC00276H.

48. G. Wang, Q. Yao, J. Dong, et al., "In Situ Construction of Multifunctional Surface Coatings on Zinc Metal for Advanced Aqueous Zinc–Iodine Batteries," *Advanced Energy Materials* 14 (2024): 2303221, https://doi.org/10.1002/aenm.202303221.

49. J. L. Yang, H.-H. Liu, X.-X. Zhao, et al., "Janus Binder Chemistry for Synchronous Enhancement of Iodine Species Adsorption and Redox Kinetics Toward Sustainable Aqueous Zn–I_2 Batteries," *Journal of the American Chemical Society* 146 (2024): 6628–6637, https://doi.org/10.1021/jacs.3c12638.

50. W. Cao, T. Hu, Y. Zhao, et al., "Tailoring C 3 N 4 Host to Enable a High-Loading Iodine Electrode for High Energy and Long Cycling Zn–Iodine Battery," *ACS Energy Letters* 10 (2025): 320–329, https://doi.org/10.1021/acsenergylett.4c02930.

51. K. Wang, H. Li, Z. Xu, et al., "An Iodine-Chemisorption Binder for High-Loading and Shuttle-Free Zn–Iodine Batteries (Adv. Energy Mater. 17/2024)," *Advanced Energy Materials* 14 (2024): 2470073, https://doi.org/10.1002/aenm.202470073.

Supporting Information

Additional supporting information can be found online in the Supporting Information section.

Supporting File 1: adma73037-sup-0001-SuppMat.docx.

Supporting File 2: adma73037-sup-0002-VideoS1.mp4.